

Article

Performance Analysis of a Robust Controller with Neural Network Algorithm for Compliance Tendon–Sheath Actuation Lower Limb Exoskeleton

Haimin He, Ruru Xi * and Youping Gong 

School of Mechanical Engineering, Hangzhou Dianzi University, Hangzhou 310018, China

* Correspondence: xiruru@hdu.edu.cn

Abstract: Robotic rehabilitation of the lower limb exoskeleton following neurological injury has proven to be an effective rehabilitation technique. Developing assistive control strategies that achieve rehabilitative movements can increase the potential for the recovery of the motor coordination of the participants. In this paper, the innovative contributions are to investigate a robust sliding mode controller (SMC) with radials basis function neural network algorithm (RBFNN) compensator for a novel compliance tendon–sheath actuation lower limb exoskeleton (CLLE) to provide intrinsic thigh and shank rehabilitation training. The controller employing the RBFNN compensator is proposed to reduce the impact of friction from the compliance tendon–sheath actuation system (CTSA). In the design of the compensator, a single parameter is investigated to replace the weight information of the neural network. Our proposed controller is shown to yield fast, stable, and accurate control performance regardless of uncertainties interaction. Two additional algorithms, including a robust adaptive sliding mode controller (RASMC) and a sliding mode proportional-integral controller (SMPIC), are introduced in this paper for comparison. The simulations were presented with MATLAB/SIMULINK to validate the superiority of the performance of the proposed controller.



Citation: He, H.; Xi, R.; Gong, Y. Performance Analysis of a Robust Controller with Neural Network Algorithm for Compliance Tendon–Sheath Actuation Lower Limb Exoskeleton. *Machines* **2022**, *10*, 1064. <https://doi.org/10.3390/machines10111064>

Academic Editor: Jan Awrejcewicz

Received: 13 September 2022

Accepted: 8 November 2022

Published: 11 November 2022

Publisher's Note: MDPI stays neutral with regard to jurisdictional claims in published maps and institutional affiliations.



Copyright: © 2022 by the authors. Licensee MDPI, Basel, Switzerland. This article is an open access article distributed under the terms and conditions of the Creative Commons Attribution (CC BY) license (<https://creativecommons.org/licenses/by/4.0/>).

Keywords: exoskeleton robot; robust control; neural network; compliance tendon–sheath actuation; uncertainties and friction

1. Introduction

Due to the fact that the problem of the aging population is increasing and the cost of artificial rehabilitation training is rising, lower limb exoskeleton robots for rehabilitation have become a current interest of researchers [1–3]. In the past, rehabilitation training for impaired lower limbs was mainly undertaken by physiotherapists, which is a labor-intensive task. Various rigid exoskeletons have been extensively implemented to free physiotherapists from heavy workloads and boost the rehabilitation training level of lower limbs in the past two decades [4], Ekso [5] and HAL [6] are representatives of them. These lower limb exoskeleton robots have similar lower limbs structure to humans, with a robotic joint axis that matches the joint axis of the human lower limb. The rigid structure allows the exoskeleton to determine the lower limb posture of the wearer and to ensure that the controlled torque is applied to each joint separately. However, some substantial deficiencies in rigid structural exoskeletons, such as their large weight, high inertia, and joint misalignment, seriously affect practicality and safety. The above-proposed prototypes do not address this issue.

In follow-up studies, flexible transmission systems, such as CTSA, have been employed in [7–9] to separate the actuator from the exoskeleton to reduce the bodyweight of the exoskeleton. In [10–12], soft exoskeletons based on CTSA, which are lightweight and have lower inertia, were developed to assist the rehabilitation of patients. The field of research for compliance tendon–sheath actuation lower limb exoskeleton is worthy of investigation. In the literature, the friction problem caused by CTSA was also introduced,

which is the main issue for engineering applications. The friction of CTSA is caused by the changing of the tendon–sheath bending angle, which renders the torque and displacement transmission of CTSA difficult. Proposing a robust control strategy that can describe and manage these uncertainties in a lower limb exoskeleton has been a central concern of researchers.

Controllers are essential for both upper and lower limb exoskeleton robots [13–15]. Wu et al. [16] investigated a tendon–sheath-actuated exoskeleton with an anthropomorphic structure using the PID method. The robust adaptive PD controller and the fuzzy PID controller for tracking the trajectory and assisting in the rehabilitation of the exoskeleton were proposed by Rosales Luengas et al. [17] and Sharma R et al. [18]. Many attempts have been made to implement SMC in an exoskeleton system. In [19], a learning control scheme for an upper-limb exoskeleton via the adaptive SMC technique was proposed to accomplish passive rehabilitation therapy tasks for the wearable six-degrees of freedom (DOF) upper limb exoskeleton. Amir Razzaghian [20] investigated a novel fractional-order Lyapunov-based robust SMC based on a fuzzy neural network compensator for exoskeleton robotic systems, which can improve the closed-loop system accuracy. Wu Q et al. [21] investigated a higher-order perturbation observer to estimate unknown composite perturbations and combined it with an adaptive sliding mode controller (ASMC) to achieve the rehabilitation of the human body. In the literature [22], a self-adaptive-coefficient double-power SMC combined with an estimated dynamic model was investigated to eliminate disturbances during operation due to environmental factors. The above studies show that the uncertainties are relatively pronounced in the exoskeleton system. For the lower limb exoskeleton based on CTSA, approaches that can effectively eliminate the effects of not only uncertainties but also friction are extremely required. In this paper, an SMC that employs neural networks was proposed to approximate and compensate for friction and uncertainties, which can effectively improve the engineering value of an exoskeleton based on CTSA.

Neural networks with function-learning capabilities can effectively simplify complex mathematical analysis problems and are effective methods to solve nonlinear control problems. In the literature [23], a sliding mode controller based on an adaptive higher-order neural network has been proposed for realizing precise position-tracking control of a hydraulic rotary drive joint. In [24], a Genetic Algorithm–Back propagation (GA–BP) neural network was proposed to estimate the motion intention of the wearer through electromyography (EMG) signals. Radial basis function neural networks (RBFNN), as one branch of neural networks, can effectively improve the performance of controllers in control of multiple-input–multiple-output (MIMO) nonlinear systems. In [25,26], adaptive RBFNN controllers were investigated for the class of MIMO nonlinear robot manipulators. Liu. Q et al. [27] investigated two kinds of adaptive bias RBFNN control schemes, which are the local bias scheme and the global bias scheme, to remedy the negative influence of the bias of the dynamics. In [28], a novel neural output feedback trajectory tracking controller for robotic exoskeletons was proposed. However, up to now, few researchers have utilized RBFNN to approximate time-varying friction and the uncertainties of lower limb exoskeletons, which possess ample potential and prospects.

Thus, the innovation of this paper is to investigate a robust adaptive SMC with an RBFNN compensator to approximate and compensate for the uncertainties and time-varying friction. Moreover, the model of the CLLE is developed, and the model information for the hip and knee joints have been analyzed. In the compensator design, a single parameter is investigated to replace the weight information of the neural network, which implements adaptive control based on parameter estimation and can effectively simplify the adaptive algorithm.

The structure of this paper can be divided into the following parts: In Section 2, the model of CLLE is analyzed and developed. In Section 3, an adaptive SMC with RBFNN compensator is investigated, and the stability is proven by employing the Lyapunov method. The model information and the specific parameters of the controllers

are introduced in Section 4. Section 5 shows the parameters of the numerical simulations. Sections 6 and 7 provides the results and discussions at the end.

2. Description and Modeling of CLLE

In this section, the model of CLLE is investigated by combining it with two models: the dynamic model and the friction model. The dynamic model is used to describe the relationship between the joint angles and the torque applied to the joints. The friction model is used to describe the frictional consumption of the CTSA.

2.1. Dynamic Model and Friction Model

The Newton–Euler method and the Lagrangian formulas have been used to discover the dynamic model of the system by preceding researchers [29]. The behavior of the lower limb exoskeletons model can be effectively described with the aid of Lagrangian approaches. The dynamic equations for the hip and knee joints in the sagittal plane can be derived from the Lagrangian method. Figure 1 shows a schematic diagram of the simplified mechanical structure of the lower limb exoskeleton, where each leg consists of 3-DOF and the DOF of the ankle is passive. The dynamics of the model are also depicted in Figure 1; the hip and knee angles are considered to be θ_1 and θ_2 , respectively.

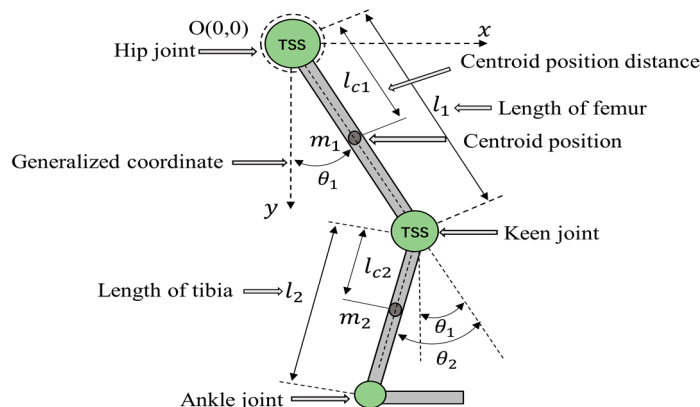


Figure 1. The simplified mechanic structure schematic of CLLE consists of two active DOFs and one passive DOF in each leg. The hip joint drives the thigh, the knee joint drives the shank, and the ankle joint is passively driven by the foot for rehabilitation training. Where l_1 and l_{c1} are the length of thigh and the distance of centroid position from knee joint, l_2 and l_{c2} are the length of shank and the distance of centroid position from knee joint. m_1 and m_2 are the mass of thigh linkage and shank linkage, θ_1 and θ_2 are the initial angle of joints.

According to the Lagrange formula and refs [29], K and P are given as the total kinetic and potential energy of the system, the Equation is given as follows:

$$L = K_{\theta_i} - P_{\theta_i} \tag{1}$$

$$T_i = \frac{d}{dt} \left(\frac{\partial L}{\partial \dot{\theta}_i} \right) - \left(\frac{\partial L}{\partial \theta_i} \right) \tag{2}$$

where L is the Lagrange function, K_{θ_i} and P_{θ_i} are the total kinetic and potential energy of the system, respectively. T_i represents the actual torques applied to the hip and knee joints, θ_i and $\dot{\theta}_i$, indicating the rotation angle and angular velocity of the joints, respectively, where $i = 1, 2$. The total kinetic and potential energy can be calculated and written as follows:

$$E_{K_{\theta_i}} = \sum_{i=1}^2 \left(\left[\frac{1}{2} I_i \dot{\theta}_i^2 + \frac{1}{2} m_i (\dot{x}_i^2 + \dot{y}_i^2) \right] \right) \tag{3}$$

$$E_{p_{\theta_i}} = \sum_{i=1}^2 (m_i y_i g) \tag{4}$$

where $i = 1, 2$, m_i denotes the mass of the thigh and shank and I_i denotes the rotational inertia. x_i and y_i are the centroid position of the linkage. \dot{x}_i and \dot{y}_i are the centroid velocity of the thigh and shank in the horizontal and vertical orientation, which can be derived from the geometric relationship of the robotic model. Based on the above formulas (1)–(4), the dynamic model in the sagittal plane is given as follows:

$$T = M(\theta)\ddot{\theta} + C(\theta, \dot{\theta})\dot{\theta} + G(\theta) + \tau \tag{5}$$

where T denotes the 2×1 vector of the torque applied to the two active joints, $\theta = [\theta_1 \ \theta_2]$, $M(\theta) \in R^{2 \times 2}$ denotes the symmetric positive definite inertia matrix, the $C(\theta, \dot{\theta}) \in R^{2 \times 2}$ denotes the Coriolis and centripetal matrix, τ denotes the external disturbances, and $G(\theta) \in R^{2 \times 1}$ represents the gravity vector.

In [30–34], previous researchers have analyzed the characteristic of CTSA. A diagram of the overall structure of the double tendon–sheath system applied to CTSA is shown in Figure 2. As shown in Figures 1 and 2, the complete CLLE structure mainly consists of four units of double tendon–sheath systems. Each leg of the exoskeleton consists of two compliant tendon–sheath drive units located at the back of the waist above the belt and brace, four tendon–sheath supports, four anchor points, and two guidance mechanisms. In this study, CTSA [21,34] is used for actuation in the lower limb exoskeleton.

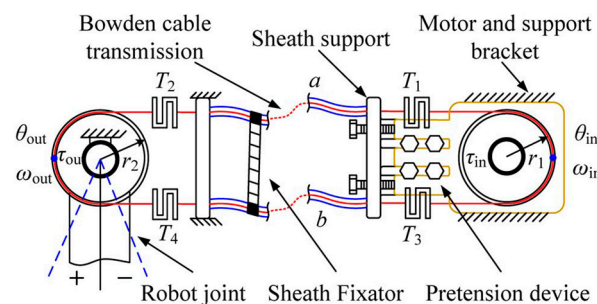


Figure 2. The schematic diagram of a double tendon–sheath. In the figure, tendons a and b are attached to the input side pulley and output side pulley with a pull–pull configuration τ_{in} and τ_{out} are the input and output torque, θ_{in} and θ_{out} are the input and output angles, ω_{in} and ω_{out} are the angular velocities of input and output, and r_1 and r_2 are the radius of the pulleys. The tendon transmits the force and torque by mechanical displacement in the inner tendon.

For the double tendon–sheath system, assuming that the elongation of the tendon in the double tendon–sheath system keeps within the elastic limit, it can be concluded that the elongation summation of tendons a and b approaches zero. According to previous research [34,35], the friction model in the transmission system can be obtained as follows:

$$F(\Theta, \dot{\theta}) = \begin{cases} \text{sign}(\dot{\theta}) 2T_0 r_1 \mu \Theta, & \dot{\theta}(t) \neq 0 \\ F(\Theta, \dot{\theta})(t^{-1}), & \dot{\theta}(t) = 0 \end{cases} \tag{6}$$

where T_0 is the pretension of the initial tendon–sheath system, and $F(\theta, \dot{\theta})(t^{-1})$ are the friction torque at a moment before t . μ denotes the friction constant between the tendons and sheaths. Θ represents the bending angle of the CTSA system, which is hard to obtain in engineering applications.

2.2. Model of CLLE

Figure 3 demonstrates the basic structure of the CLLE, including the electrical part, transmission part, and mechanical part. In Figure 3, U_m represents the input voltage of the DC motor, T_m is the input torque of the transmission system, and T represents the torque applied on each joint. In this paper, the discussion mainly focuses on the controller that eliminates the negative friction effects, so the details of the electrical part will not be analyzed.

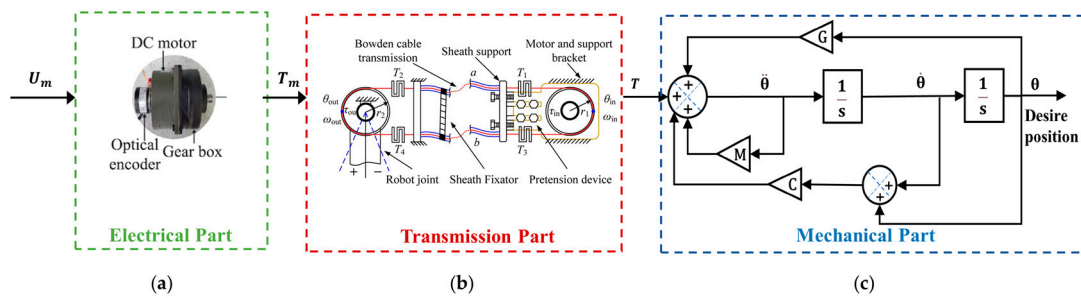


Figure 3. The block diagram of CLLE. (a) DC motor and encoder of the electrical part; (b) the transmission system of the CTSA; (c) the block diagram of mechanical part.

From Figure 3, the torque T , which is applied to the joints can be expressed as $T = T_m - F(\Theta, \dot{\theta})$. Substituting it into Equations (5) and (6), the model of CLLE is given as follows:

$$T_m = M(\theta)\ddot{\theta} + C(\theta, \dot{\theta})\dot{\theta} + G(\theta) + \tau + F(\Theta, \dot{\theta}) \tag{7}$$

According to Equations (6) and (7), it can be inferred that the radius of the pulleys, the pretension of the tendon, the total bending angle, and the friction coefficient are the main factors that determine the characteristics of torque transmission. Nevertheless, in practical application, the bending angle of CTSA will constantly change during operation, which will lead to notable variations in torque transmission. Meanwhile, it is hard to construct a real-time measurement system for detecting changes in the bending angle. Therefore, in order to eliminate the effects, a robust adaptive SMC with RBFNN compensator is proposed. The proposed controller can significantly approximate time-varying friction and satisfy the demands of CLLE.

3. Controller Design

Sliding mode controllers (SMC) are popular in robotic control systems [36]. In this section, a robust adaptive SMC with an RBFNN algorithm compensator was introduced to eliminate the effects of uncertainties and friction in the CLLE. The universal approximation characteristic of RBFNN was utilized to enable SMC to implement enhanced performance. Figure 4 shows the scheme of SMC with the compensator.

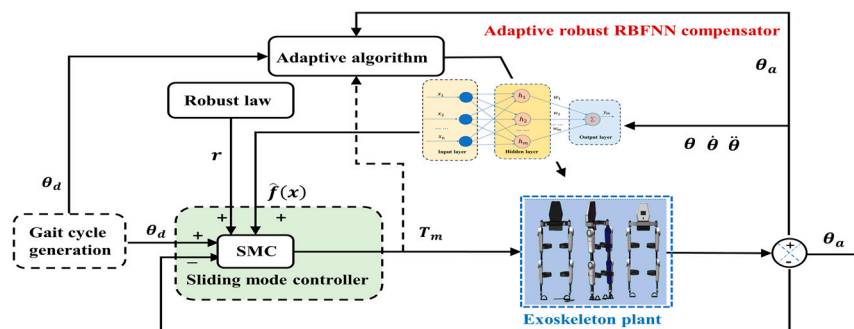


Figure 4. Scheme of SMC with robust adaptive RBFNN compensator.

3.1. SMC Design

The desired and actual angle position are defined as θ_d and $\theta(t)$ and the desired trajectories error as $e(t)$, which can be expressed as follows:

$$e(t) = \theta_d(t) - \theta(t) \tag{8}$$

The sliding mode function, s , can be defined as follows:

$$s = \dot{e}(t) + \lambda e(t) \tag{9}$$

Differentiating e with respect to t and substituting it into Equation (9) can obtain the following:

$$s = \dot{\theta}_d(t) - \dot{\theta}(t) + \lambda e(t) \tag{10}$$

Differentiate s with respect to t ,

$$\dot{s} = \ddot{\theta}_d(t) - \ddot{\theta}(t) + \lambda \dot{e}(t) \tag{11}$$

Multiply both sides of the Equation by the matrix $M(\theta)$ at the same time and substitute Equation (7) into it, then Equation (11) can be rewritten as follows:

$$\begin{aligned} M(\theta)\dot{s} &= M(\theta)\left(\ddot{\theta}_d + \lambda\dot{e}\right) + C\dot{\theta} + G(\theta) + F(\Theta, \dot{\theta}) + \tau - T_m \\ &= M(\theta)\left(\ddot{\theta}_d + \lambda\dot{e}\right) + C\left(\dot{\theta}_d + \lambda e\right) - C \cdot s + G + F(\Theta, \dot{\theta}) + \tau - T_m \end{aligned} \tag{12}$$

The uncertain terms in Equation (12) can be defined as a tag function f , which can be written as follows:

$$f = \Delta M(\theta)\left(\ddot{\theta}_d + \lambda\dot{e}\right) + \Delta C\left(\dot{\theta}_d + \lambda e\right) + \Delta G + F(\Theta, \dot{\theta}) \tag{13}$$

where the tag function f includes the modeling errors terms ΔM and ΔC , the disturbances term ΔG and time-varying friction term $F(\Theta, \dot{\theta})$, respectively. The tag function f is unknown and needs to be approximated. The neural network learning method is adopted here, the upper bound estimated value of the neural network is taken as the estimated value of the neural network, and the adaptive law of parameter estimation is used to replace the weight adjustment of the neural network for approximating the tag function f .

3.2. Neural Network Framework

The control system for CLL robots can be regarded as a multi-input and multi-output (MIMO) model system. For the MIMO system, the neural network is capable of learning complex models online or offline through forward and reverse dynamic behaviors by adapting to changes in the environment design. The RBFNN is investigated here as a controller compensator. As shown in Figure 5, the radial basis function neural network consists of three layers, which are the input layer, hidden layer, and output layer, respectively.

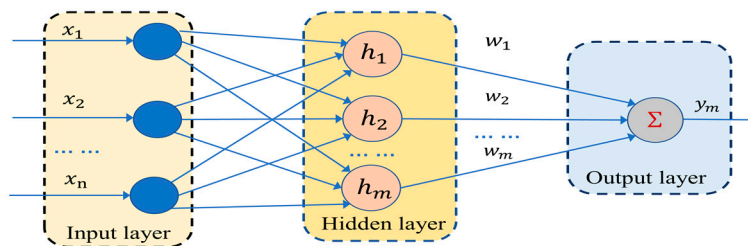


Figure 5. Structure of radial basis function neural network.

The neuron activation function of the hidden layer is composed of radial basis functions, and the array operation unit is the hidden layer node. Each hidden layer node includes a center vector with the same dimension as the input parameter vector. The nonlin-

ear activation function is designed for the output of the hidden layer as $h_j(t)$, which can be expressed as follows:

$$h_j(t) = \exp\left(-\frac{\|x_j(t) - c_j(t)\|^2}{2b_{ij}^2}\right), \quad i, j = 1, \dots, m \quad (14)$$

where b_{ij} is a positive scalar representing the width of the Gaussian function and m is the number of hidden layer nodes. c_j , the coordinate vector of the center of the Gaussian function in the hidden layer neuron. $x_j(t)$ denotes the network input signal. The Weighting function, $y_i(t)$, is investigated to achieve neural network output, which can be defined as follows:

$$y_i(t) = \sum_{j=1}^m w_{ji} h_j(t), \quad i = 1, \dots, n \quad (15)$$

where w is the weight of the output layer, n and y_i represent the number of the output layer nodes and the output of the neural network. A radial basis function neural network was constructed to approximate the function f , the specific method is as follows, define f in a neural network as follows:

$$f_i = W^T h_i(t) + \varepsilon \quad (16)$$

where $W \in R^{1 \times m}$ represents the vector of the weight of the output layer. ε indicates the neural network approximation error, which is assumed to be $|\varepsilon| \leq \varepsilon_N$. According to the output of the neural network and function f in the neural network, assuming that the estimated value of function f of the neural network is defined as \hat{f}_i , it can be written as follows:

$$\hat{f}_i = W_i^T h_i(t) + \varepsilon \quad (17)$$

3.3. Control Law

According to the estimated value of function f of the neural network in Section 3.2 and the model of CLLE, f_i and \hat{f}_i can be defined as follows:

$$f(x) = [f_1 \quad f_2]^T = \begin{bmatrix} w_1^T h_1 + \varepsilon_1 \\ w_2^T h_2 + \varepsilon_2 \end{bmatrix} = \begin{bmatrix} w_1^T h_1 \\ w_2^T h_2 \end{bmatrix} + \varepsilon \quad (18)$$

where $\varepsilon = [\varepsilon_1 \quad \varepsilon_2]^T$. According to Equations (14) and (18), the network input signals were defined as $x_i = [e_i \quad \dot{e}_i \quad q_{di} \quad \dot{q}_{di} \quad \ddot{q}_{di}]$ and $x = [x_1 \quad x_2]^T$, where $i = 1, 2$ denotes the number of joints.

The weight of the output layer was defined as $w_1 \quad w_2$ and the estimated weight value as $\hat{w}_1 \quad \hat{w}_2$. Assuming that the error of the weight function is \tilde{w} ,

$$\tilde{w} = \begin{bmatrix} w_1 - \hat{w}_1 \\ w_2 - \hat{w}_2 \end{bmatrix}, \quad \|w_i\|_F \leq \max\{w_1 \cdot w_2\} \quad (19)$$

Taking a normal number, φ , which can be defined as $\varphi = \max_{i=1,2} \{\|w_i\|^2\}$ and $\tilde{\varphi} = \hat{\varphi} - \varphi$, $\hat{\varphi}$, represents the estimated value of φ . The control law is investigated as follows:

$$T_m = \frac{1}{2} \hat{\varphi} s^T h_1 + k_v s - r \quad (20)$$

where k_v denotes the control parameter and r represents the robust term for overcoming the approximation error of the neural network. r can be defined as $r = -(\varepsilon_N + b_d) \text{sgn}(s)$. Substituting Equations (13) and (20) into Equation (12), the following can be obtained:

$$M(\theta) \dot{s} = -(k_v + C)s - \frac{1}{2} \hat{\varphi} s \cdot h_1^T h_1 + (f + \tau) + r \quad (21)$$

The formula in Equation (9) defines that $S = [s_1 \ s_2]^T$, $E(t) = [e_1 \ e_2]^T$, $\dot{E}(t) = [\dot{e}_1 \ \dot{e}_2]^T$ and $\lambda' = \begin{bmatrix} \lambda_1 & \\ & \lambda_2 \end{bmatrix}$, $\lambda_1, \lambda_2 > 0$. Then Equation (9) can be described as $S = E(t) + \lambda' \dot{E}(t)$. Based on Equation (18) and the model of CCLE, the following can be obtained:

$$M(\theta)\dot{S} = -(k_v + C)S - \frac{1}{2}\hat{\varphi}S \circ H + (f + \tau) + r \tag{22}$$

where $H \in R^{1 \times 2} = [h_1^T h_1 \ h_2^T h_2]^T$ denotes the nonlinear activation function of joints. $S \circ H$ can be expressed as, $S \circ H = [s_1 h_1^T h_1 \ s_2 h_2^T h_2]^T$.

3.4. Proof of Lyapunov Stability

A Lyapunov function V is designed as follows:

$$\begin{cases} V = V_1 + V_2 \\ V_1 = \frac{1}{2}S^TMS \\ V_2 = \frac{1}{2}\frac{1}{\beta}\varphi^2 \end{cases} \tag{23}$$

Calculating the derivative of the first term V_1 , one obtains the following:

$$\begin{aligned} \dot{V}_1(t) &= \frac{1}{2}\dot{S}^TMS + \frac{1}{2}S^T\dot{M}\dot{S} + \frac{1}{2}S^T\dot{M}\dot{S} \\ &= S^T \left[-(k_v + C)S - \frac{1}{2}\hat{\varphi}S \circ H + (f + \tau_d) + r \right] + \frac{1}{2}S^T\dot{M}\dot{S} \\ &= S^T \left[-K_vS - \frac{1}{2}\hat{\varphi}S \circ H + W_h + (\varepsilon + \tau_d + r) \right] + \frac{1}{2}S^T(\dot{M} - 2C)S \\ &= S^T \left[-\frac{1}{2}\hat{\varphi}S \circ H + W_h \right] - S^T k_v S + S^T(\varepsilon + \tau_d + r) \end{aligned} \tag{24}$$

where $W_h = [w_1^T h_1 \ w_2^T h_2]^T$. $M(\theta) \in e \times 2$ denotes the symmetric positive definite inertia matrix, and based on the Matrix characteristics, the following is obtained:

$$S^T(\dot{M} - 2C)S = 0 \tag{25}$$

Therefore, it can be defined as follows:

$$S^T(\varepsilon + \tau_d + r) = S^T(\varepsilon + \tau_d - (\varepsilon_N + b_d)\text{sgn}(s)) \leq 0 \tag{26}$$

Let $S^T k_v S \geq 1$, one obtains,

$$\begin{aligned} S^2 \varphi h_i^T h_i + 1 &= S^2 \|W\|^2 h_i^T h_i + 1 \\ &= S^2 \|W\|^2 \|h_i\|^2 + 1 \\ &= S^2 \|W^T h_i\|^2 + 1 \geq 2SW^T h_i \end{aligned} \tag{27}$$

Thus, $\frac{1}{2}S^2 \|W^T h_i\|^2 + \frac{1}{2} \geq SW^T h_i$. Since $S^T W_h = [s_1 \ s_2] [w_1^T h_1 \ w_2^T h_2]^T = \sum s_i w_i^T h_i$ ($i = 1, 2$). According to Equation (27), we achieve,

$$S^T W_h \leq \frac{1}{2}\varphi \sum s_i w_i^T h_i (i = 1, 2) + \frac{n}{2} \tag{28}$$

From Equation (22), $S^T \left[-\frac{1}{2}\hat{\varphi}S \circ H \right]$ can also be transferred to

$$\begin{aligned} S^T \left[-\frac{1}{2}\hat{\varphi}S \circ H \right] &= -\frac{1}{2}\hat{\varphi}[s_1 s_2] \begin{bmatrix} s_1 h_1^T h_1 \\ s_2 h_2^T h_2 \end{bmatrix} = -\frac{1}{2}\hat{\varphi} \left(s_1^2 \|h_1\|^2 + s_2^2 \|h_2\|^2 \right) \\ &= -\frac{1}{2}\hat{\varphi} \sum_{i=1}^n s_i^2 \|h_i\|^2 \end{aligned} \tag{29}$$

Thus, $S^T \left[-\frac{1}{2} \hat{\varphi} S \circ H \right] \leq 0$ is satisfied. As $\dot{V}_2 = \frac{1}{\beta} \tilde{\varphi} \dot{\hat{\varphi}}$, we obtain,

$$\begin{aligned} \dot{V} = \dot{V}_1 + \dot{V}_2 &\leq -\frac{1}{2} \hat{\varphi} \sum_{i=1}^n s_i^2 \|h_i\|^2 + \frac{1}{2} \varphi \sum_{i=1}^n s_i^2 h_i^T h_i + \frac{n}{2} + \frac{1}{\beta} \tilde{\varphi} \dot{\hat{\varphi}} - S^T K_v S \\ &= -\frac{1}{2} \tilde{\varphi} \sum_{i=1}^n s_i^2 \|h_i\|^2 + \frac{n}{2} + \frac{1}{\beta} \tilde{\varphi} \dot{\hat{\varphi}} - S^T K_v S \\ &= \tilde{\varphi} \left(-\frac{1}{2} \sum_{i=1}^n s_i^2 \|h_i\|^2 + \frac{1}{\beta} \dot{\hat{\varphi}} \right) + \frac{n}{2} - S^T K_v S \end{aligned} \quad (30)$$

Then the adaptive control law is investigated as follows:

$$\dot{\hat{\varphi}} = \frac{\beta}{2} \sum_{i=1}^n s_i^2 \|h_i\|^2 \quad (31)$$

The A Lyapunov function V can be rewritten as follows:

$$\dot{V} = \frac{n}{2} - S^T K_v S \quad (32)$$

Considering that the model of CLLE, $n = 2$ is determined. From Equations (30) and (32), one obtains the following:

$$\dot{V} = \frac{n}{2} - S^T k_v S = 1 - S^T k_v S \quad (33)$$

To ensure the Lyapunov function V and $\dot{V} \leq 0$, we can define the parameter of k_v to make $\frac{n}{2} \leq S^T k_v S$ stand. Therefore, we obtain the following:

$$\dot{V} \leq \frac{n}{2} - S^T k_v S \leq 0 \quad (34)$$

Therefore, the Lyapunov function V will continuously decrease, and the system will be stable. Then the proposed controller of the CLEE system is convergent and stable over time.

4. Model and Controller Identification

4.1. Model Parameters Identification

The model of CLLE is proposed in Equation (7). Actually, the parameters $M(\theta)$, $C(\theta)$, and $G(\theta)$ are formulated in the following specific form.

$$\begin{aligned} M(\theta) &= \begin{bmatrix} I_1 + I_2 + m_1 l_{c1}^2 + m_2 l_1^2 + m_2 l_{c2}^2 + 2m_2 l_1 l_{c2} \cos \theta_2 & I_2 + m_2 l_{c2}^2 + m_2 l_1 l_{c2} \cos \theta_2 \\ I_2 + m_2 l_{c2}^2 + m_2 l_1 l_{c2} \cos \theta_2 & I_2 + m_2 l_{c2}^2 \end{bmatrix} \\ C(\theta) &= \begin{bmatrix} -2m_2 l_1 l_{c2} \sin \theta_2 \cdot \dot{\theta}_2 & -m_2 l_1 l_{c2} \sin \theta_2 \cdot \dot{\theta}_2 \\ m_2 l_1 l_{c2} \sin \theta_2 \cdot \dot{\theta}_1 & 0 \end{bmatrix} \\ G(\theta) &= \begin{bmatrix} -m_1 g l_{c1} \sin \theta_1 - m_2 g l_1 \sin \theta_1 - m_2 g l_{c2} \sin(\theta_1 + \theta_2) + d_1 \\ -m_2 g l_{c2} \sin(\theta_1 + \theta_2) + d_2 \end{bmatrix} \end{aligned} \quad (35)$$

where $I_i (i = 1, 2)$ denotes the moment of inertia with the rectus thighs and shank, g denotes the gravitational acceleration, and d_1 and d_2 represent the external disturbance of gravity on the thigh and shank, respectively.

4.2. Design of SMPIC and RASMC

The superiority of the proposed method is demonstrated when compared with the other two controllers. The classic sliding mode proportional-integral controller (SMPIC) and the robust adaptive sliding mode controller (RASMC) are chosen.

SMPIC was designed as follows. Define $e'(t) = \theta_d(t) - \theta(t)$ and $s' = \dot{e}'(t) + \gamma e'(t)$. Assuming that $E'(t) = [e'_1 \ e'_2]^T$, $\dot{E}'(t) = [\dot{e}'_1 \ \dot{e}'_2]^T$, $\gamma' = \begin{bmatrix} \gamma_1 & \\ & \gamma_2 \end{bmatrix}$, $\gamma_1, \gamma_2 > 0$. Therefore, the law of SMPIC is designed as follows:

$$T'_m = T + k_p s' + k_i \int s' dt + \tau_s \quad (36)$$

where k_p and k_i are the proportional gain and the integral gain, which are $k_p > 0$ and $k_i > 0$. τ_s represents the robust term and $\tau_s = k_{s'} \text{sgn}(s')$. Substituting it into Equation (12), we can obtain the following:

$$M(\theta) \dot{S}' + C(\theta, \dot{\theta}) S' + k_i \int_0^t s' dt = -k_p s' - k_{s'} \text{sgn}(s') + E_S \quad (37)$$

where E denotes the joint angle error of CCLE and $S' = [s'_1 \ s'_2]^T$. Lyapunov function V is investigated as follows:

$$V = \frac{1}{2} S'^T M S' + \frac{1}{2} \left(\int_0^t s' d\tau \right)^T k_i \left(\int_0^t s' d\tau \right) \quad (38)$$

Calculating the derivative of the first term V , one obtains the following:

$$\dot{V} = S'^T \left[M \dot{S}' + \frac{1}{2} \dot{M} S' + k_i \int_0^t s' dt \right] \quad (39)$$

Considering the symmetry of the matrix, we find $S'^T (\dot{M} - 2C) S' = 0$, thus the equation can be rewritten as follows:

$$\dot{V} = S'^T \left[M \dot{S}' + \frac{1}{2} \dot{M} S' + k_i \int_0^t s' dt \right] \quad (40)$$

Due to $k_{s'} = \text{diag}[k_{ii}]$, we can define that $k_{s'} \text{sgn}(s) \geq |E_S|$. Substituting Equation (37) into Equation (40), we can obtain the following:

$$\dot{V} = -S'^T k_p S' - S'^T k_{s'} \text{sgn}(s') + S'^T E_S \quad (41)$$

Thus, we find that $\dot{V} \leq -s^T k_p s \leq 0$. So that, if $s' \equiv 0$ while $V \equiv 0$, as LaSalle's Invariance Principle, we have that when t approaches infinity ($t \rightarrow \infty$) and s' approach to zero ($t \rightarrow 0$), systematic error bounded convergence ($e' \rightarrow 0$, $\dot{e}' \rightarrow 0$), the system is asymptotically stable.

Then the RAMSC is introduced as follows for the CLLE. The control law is investigated [37] as follows:

$$T_m = \hat{H}(q) \dot{q}_r + \hat{C}(q, \dot{q}) \dot{q}_r + \hat{G}(q) + Y \hat{a} - K_D s + F(\theta, \dot{\theta}) \quad (42)$$

The adaptive law is investigated as follows:

$$\dot{\hat{a}} = -\Gamma \cdot Y^T \cdot s'' \quad (43)$$

where $q = [q_1 \ q_2]^T$ represents the angle of the thigh and shank. $\tau_a = [\tau_h \ \tau_k]^T$ denotes the torque. $s'' = \dot{e}''(t) + \zeta e''(t) = \dot{q} - \dot{q}_r$, $\dot{q}_r = q_d - \zeta e''$. Moreover, K_D , Γ , and c are all diagonal gain matrices. The stability proof of RASMC (42) and (43) can refer to former research [37].

5. Parameters and Numerical Simulations

In this section, the parameters of the numerical simulation are presented with three control methods for CLLE. Some nomenclature that is useful for the later analysis of the simulation results is described. The desired and actual angle trajectories of the hip and knee joints are defined in the former section as $\theta_d = [\theta_{d1} \theta_{d2}]^T$ and $\theta_a = [\theta_{a1} \theta_{a2}]^T$. The tracking error is defined as $e = [e_1 e_2]^T$, where $e = \theta_d - \theta_a$. The parameters of the CLLE are shown in Table 1. The length of the upper leg (l_1) can be defined as $0.2780 \cdot HT$ (height of the person, 180 cm), and the length of the lower leg (l_2) can be defined as $0.2206 \cdot HT$. The mass of the upper leg (m_1) is 0.1 MT (total mass of the person, 80 kg) and the mass of the lower leg (m_2) is 0.0405 MT. For the CLLE, refer to (6), (7), and refs [34]; the parameters of the CTSA are shown in Table 2.

Table 1. List of physical parameters in 2-DOF lower limb exoskeleton.

Parameter	Value	Parameter	Value
m_1	8 (kg)	l_{c1}	0.25 (m)
m_2	4 (kg)	l_{c2}	0.2 (m)
l_1	0.5 (m)	g	9.8 (kg·m/s ²)
l_2	0.4 (m)		

Table 2. List of physical parameters in CTSA.

Parameter	Value	Parameter	Value
T_0	80 (N·m)	μ	0.1333
Θ (initial)	Pi/2 (rad)	r_1	65 (mm)
r_2	65 (mm)		

To fully demonstrate the robustness of our proposed approach, a series of comparative numerical simulations were conducted.

Case 0: The desired trajectory for the simultaneous acquisition of CLLE performance is as follows. A simulation with uncertainties and friction is proposed in this case.

$$\theta_{d1} = 0.5 \times \sin\left(2t + \frac{\pi}{4}\right) \quad (44)$$

$$\theta_{d2} = 0.5 \times \cos\left(2t + \frac{\pi}{4}\right) \quad (45)$$

Case I: From clinical gait analysis [38], the desired trajectory for the simultaneous acquisition of CLLE performance is as follows. A simulation without uncertainties and friction is proposed in this case.

$$\theta_{d1} = \frac{[18.7 \cos(4t) - 9 \sin(4t) + 2 \cos(8t) - 5 \sin(8t) + 0.8 \cos(12t) + \sin(12t)]\pi}{180} \quad (46)$$

$$\theta_{d2} = -\frac{[23.6 + 6 \cos(4t) + 17 \sin(4t) - 10.6 \cos(8t) + 6.2 \sin(8t) - 0.6 \cos(12t) - 4.7 \sin(12t)]\pi}{180} \quad (47)$$

Case II: In this case, the desired trajectory is the same as in case1. A simulation is proposed with uncertainties and friction.

Case III: In this case, three sets of time-varying uncertainties and disturbances with different magnitudes are introduced in the simulations, namely:

$$(I) d_1 = \cos(40t) \text{ and } d_2 = \sin(40t).$$

$$(II) d_1 = 4 \cos(40t) \text{ and } d_2 = 4 \sin(40t).$$

$$(III) d_1 = 8 \cos(40t) \text{ and } d_2 = 8 \sin(40t).$$

The external disturbance can be expressed as $\tau_d = [\tau_{d1} \tau_{d2}]$. In case0 and caseII, τ_d is obtained as $\tau_{d1} = \sin(8t)$; $\tau_{d2} = \sin(6t)$, respectively. The initial hip and knee joints angle are taken as $\theta_1 = 0.5 \text{ rad}$, $\theta_2 = 0.5 \text{ rad}$, and $\dot{\theta}_1 = 0$, $\dot{\theta}_2 = 0$.

For the parameters employed in the proposed method, SMPIC and RASMC, the parameters are set as follows. In the proposed controller, define that $k_v = \text{diag}(200, 200)$, $\lambda' = \text{diag}(50, 50)$, ε_N and b_d are 0.5 and 0.2, respectively. $\beta = 500$, $M = 2$, and the thickness of the sliding mode surface is 0.01. The initial weight of the neural network is selected as the zero vector. In the SMPIC, the following can be defined, $k_p = \text{diag}(100, 100)$, $k_i = \text{diag}(80, 80)$, $k_s = \text{diag}(15, 15)$, and $\gamma' = \text{diag}(5.0, 5.0)$. In RASMC, the following can be defined, $\zeta = \text{diag}(4.0, 2.0)$, $k_d = \text{diag}(10, 10)$, and $\Gamma = \text{diag}(0.1, 0.1, 0.1, 0.1)$. The simulations were performed in MATLAB R2021a with Simulink and ode15s solver. C plus was used for the writing function, and the total simulation time was set to 10 to 15 s. In addition, the disturbance was sufficiently introduced into the simulations.

6. Results and Discussions

The performance of the three controllers under different conditions in the CLLE has been validated, and the numerical simulation results are as follows in the discussion.

Case 0: The performance of the three controllers on gait tracking in 2–DOF CLLE under uncertainty and friction was observed. The corresponding simulation results, in this case, have been exhibited in Figures 6–8 (only 0–10 s are exhibited). In Figure 6, the temporal response of the angular position of the hip and knee joints is shown. The simulation results revealed that our proposed method and SMPIC present slightly better accuracy than the RASMC in tracking the desired gait trajectories. Meanwhile, the control effects and response speed of our proposed method are superior to RASMC and SMPIC. In Figure 7, the tracking errors of the angular position of the hip and knee joints are exhibited. The proposed method possesses smoother convergence in both hip and knee joint control compared to RASMC and SMPIC. In Figure 8a,b, the time histories of the control torque of hip and knee joints have been given, which revealed that the peak input torque varies for different control algorithms.

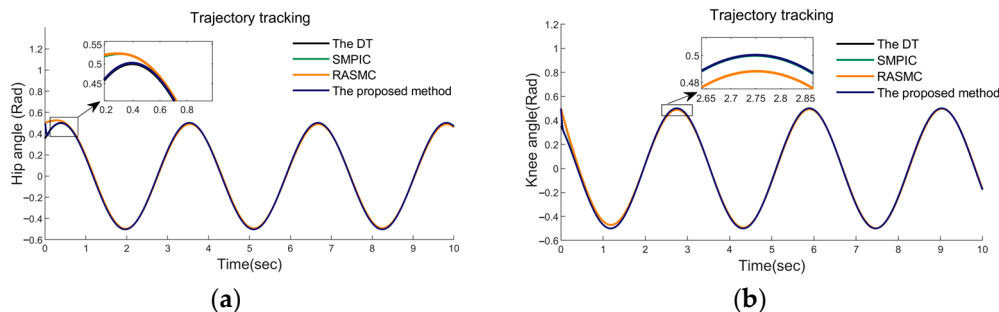


Figure 6. The tracking response of the joints. (a) the response of θ_1 under case 0 condition; (b) the response of θ_2 under case 0 condition.

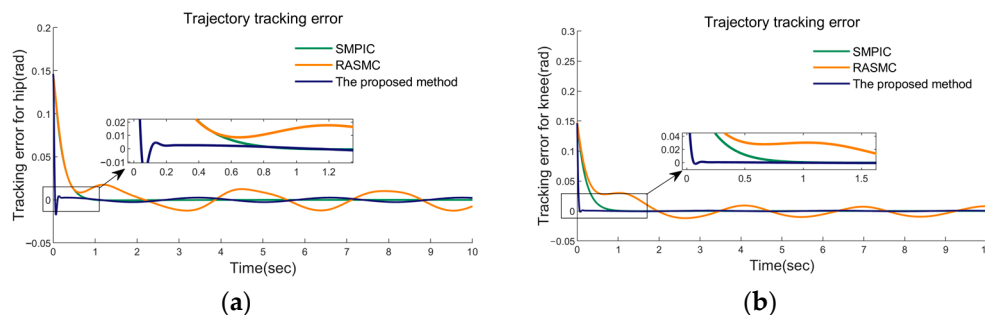


Figure 7. The tracking error of the joints. (a) the tracking error of θ_1 under case 0 condition; (b) the tracking error of θ_2 under case 0 condition.

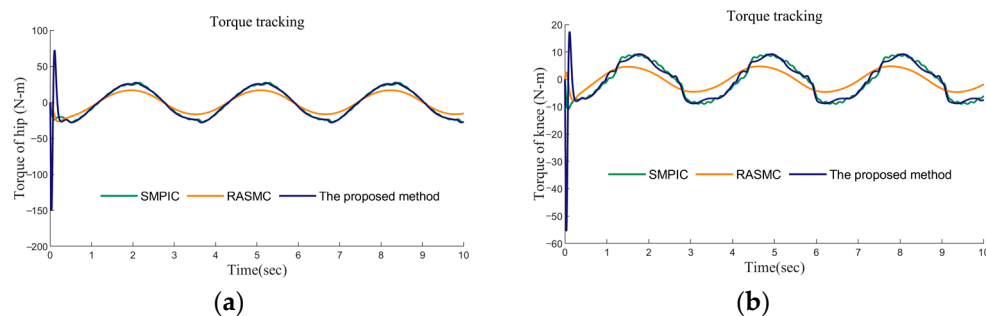


Figure 8. The time history of the joints. (a) The time history of hip torque under case 0 condition and (b) The time history of knee torque under case 0 condition.

Case I: In this case, the tracking performance of the three controllers without uncertainties and frictions was simulated. The desired gait trajectories were obtained from clinical gait analysis [38], and the results are exhibited in Figures 9–11. In this condition, all three control methods enable achieving effective trajectory tracking. Figure 9a,b clearly stated that our proposed method, SMPIC and RAMSC can achieve different gait trajectory tracking. From Figure 10, it can be concluded that the convergence of the tracking errors of the proposed method and SMPIC are superior to RASMC. In Figure 11a,b, the time histories of the control torque of hip and knee joints have been given. The input torques of three methods were smooth and can achieve soundtracking of the control torques. In conclusion, all three methods can achieve soundtracking control of the desired gait trajectory, irrespective of uncertainties and disturbances.

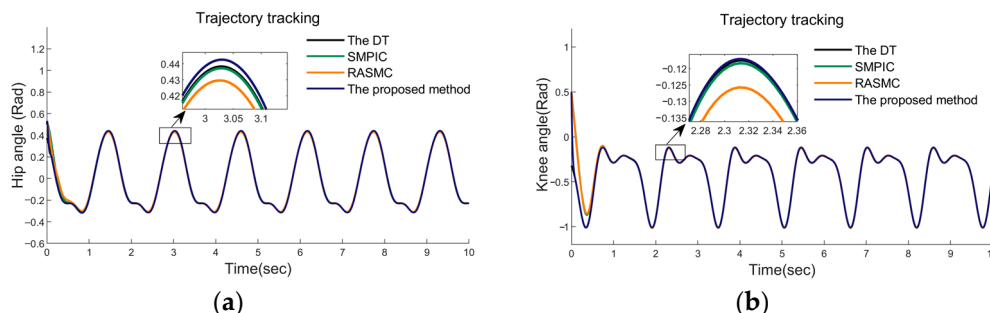


Figure 9. The tracking response of the joints. (a) the response of θ_1 under case 1 condition; (b) the response of θ_2 under case 1 condition.

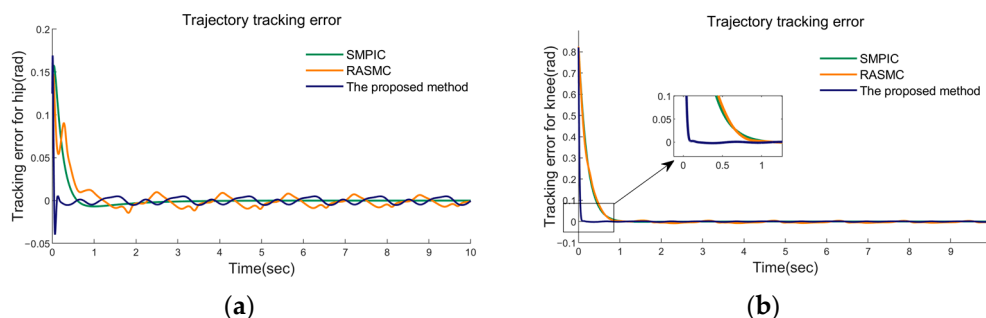


Figure 10. The tracking error of the joints. (a) the tracking error of θ_1 under case 1 condition; (b) the tracking error of θ_2 under case 1 condition.

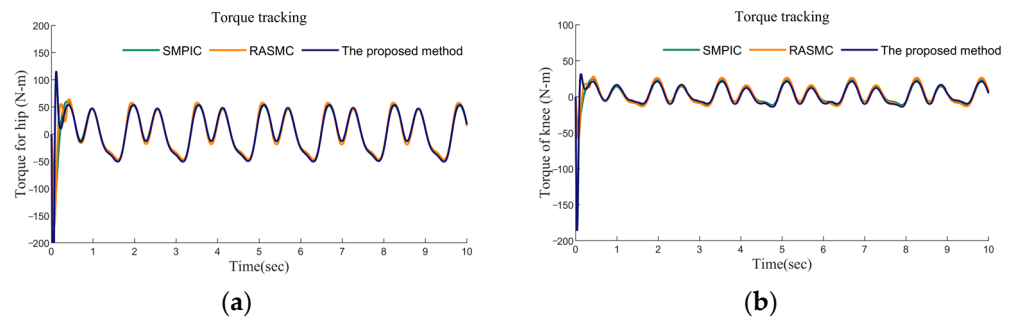


Figure 11. The time history of the joints. (a) The time history of hip torque under case 1 condition and (b) The time history of knee torque under case 1 condition.

Case II: In this case, the uncertainty and the friction of the CTSA were introduced into the numerical simulation. The results of the validation under the condition are given in Figures 12–14. Figure 12 show that our proposed method, SMPIC, and RASMC, are insensitive to both uncertainty and friction. The correspondingly soundtracking results can be effectively achieved for the desired trajectory. Figure 13a,b show a significant deterioration in hip trajectory tracking under RASMC and SMPIC. The proposed method received slightly impact by uncertainties and friction but still possesses the smooth convergence of the tracking error. Figure 14 presents the time histories of the control torque of the hip and knee joints and the control torques of our proposed method and SMPIC are much smoother than RASMC. The 2-D trajectory tracking in case0, case I, and case II of the hip and knee joints are shown in Figure 15, which further demonstrates the stable convergence of the tracking error of our proposed method, which can effectively achieve soundtracking under harsh environments.

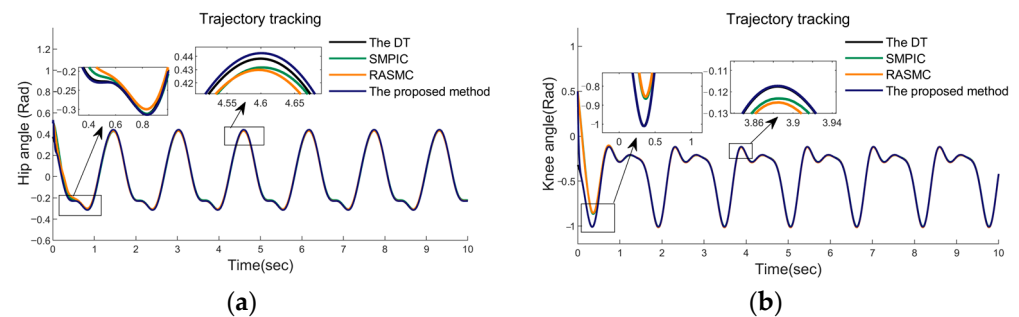


Figure 12. The tracking response of the joints. (a) the response of θ_1 under case 2 condition; (b) the response of θ_2 under case 2 condition.

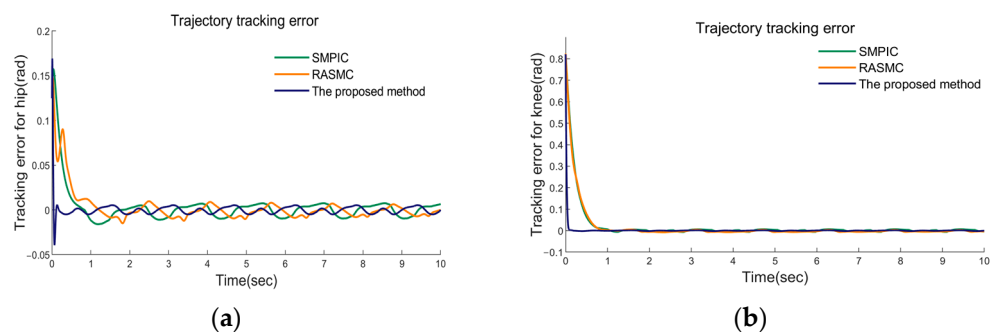


Figure 13. The tracking error of the joints. (a) the tracking error of θ_1 under case 2 condition; (b) the tracking error of θ_2 under case 2 condition.

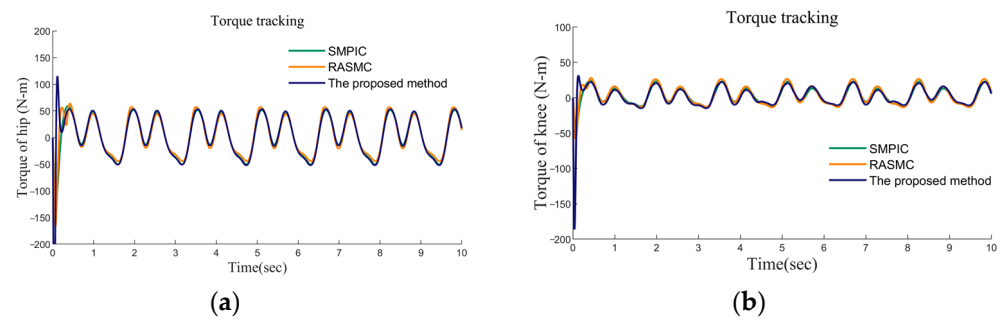


Figure 14. The time history of the joints. (a) The time history of hip torque under case 2 condition and (b) The time history of knee torque in case 2 condition.

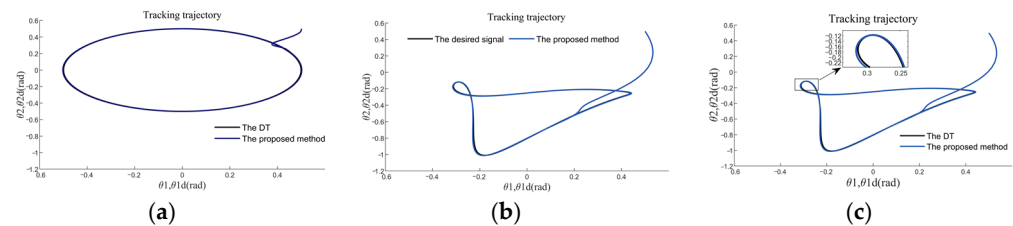


Figure 15. 2-D trajectory tracking of the hip and knee joints. (a) 2-D trajectory tracking of the hip and knee under case 0; (b) 2-D trajectory tracking under case 1; (c) 2-D trajectory tracking under case 2.

To analyze the performance of the three controllers under different conditions, the following evaluation indicators have been introduced for comparison and validation. The criteria indicators of MSE (Mean Square Error), RMSE (Root Mean Square Error), MAE (Mean Absolute Error), and MAPE (Mean Absolute Percentage Error) are proposed to validate the control performance of the three methods. Meanwhile, define the Integral Squared Error (ISE) of the hip and knee tracking as $J_{ISE} = \int_0^t e^2 dt$, which can better demonstrate the tracking performance. The results of performance criteria indicators are shown in Tables 3–5.

Table 3. The performance criteria indicators (hip, knee) under case 0 condition.

Condition Case 0	MAPE	MSE	MAE	RMSE	ISE
proposed method	(0.0087, 0.0074)	(0.0001, 0.0001)	(0.0025, 0.0012)	(0.0106, 0.0097)	(0.0112, 0.0094)
SMPIC	(0.0479, 0.0804)	(0.0003, 0.0003)	(0.0051, 0.0052)	(0.0189, 0.0198)	(0.0359, 0.0356)
RASMC	(0.0908, 0.1106)	(0.0004, 0.0005)	(0.0115, 0.0114)	(0.0208, 0.0226)	(0.0433, 0.0511)

Table 4. The performance criteria indicators (hip, knee) under case 1 condition.

Condition Case 1	MAPE	MSE	MAE	RMSE	ISE
proposed method	(0.0230, 0.0277)	(0.0001, 0.0020)	(0.0035, 0.0039)	(0.0100, 0.0457)	(0.0101, 0.2091)
SMPIC	(0.0504, 0.1575)	(0.0004, 0.0105)	(0.0049, 0.0201)	(0.0210, 0.1127)	(0.0443, 1.0549)
RASMC	(0.1074, 0.1107)	(0.0003, 0.0081)	(0.0072, 0.0184)	(0.0178, 0.0902)	(0.0316, 0.8191)

Table 5. The performance criteria indicators (hip, knee) under case 2 condition.

Condition Case 2	MAPE	MSE	MAE	RMSE	ISE
proposed method	(0.0291, 0.0255)	(0.0001, 0.0020)	(0.0040, 0.0039)	(0.0121, 0.0561)	(0.0146, 0.3147)
SMPIC	(0.0700, 0.2569)	(0.0004, 0.0105)	(0.0061, 0.0201)	(0.0321, 0.1772)	(0.0486, 1.4189)
RASMC	(0.1160, 0.1600)	(0.0004, 0.0081)	(0.0094, 0.0184)	(0.0216, 0.1103)	(0.0467, 1.2163)

As the results are shown in Tables 3–5, our proposed method demonstrates its superiority in performance criteria indicators. The following performance criteria indicators of the proposed method are significantly better than the other two methods, which proves

that our proposed method possesses outstanding precision of control and can achieve the purposes of CLLE for rehabilitation applications.

Case III: In this case, to verify the robustness of the three methods, a set of comparisons between SMPIC, RASMIC, and the proposed controller in the presence of three different amplitudes of external disturbances were introduced. The data are shown in Figures 16–18. As displayed in Figures 16 and 17, the RASMIC and SMPIC have shown an obvious deterioration in tracking performances as the external disturbances increase. However, in Figure 18, our proposed controller can still maintain an acceptable tracking control for desired gait trajectories even under such bad uncertainties and disturbances. This phenomenon validates the sound robustness of our proposed method to uncertainties and external disturbances, which is extremely necessary for engineering practice; as a bottom line, the proposed method must be in a position to preserve its robustness even under the worst influence of uncertainties.

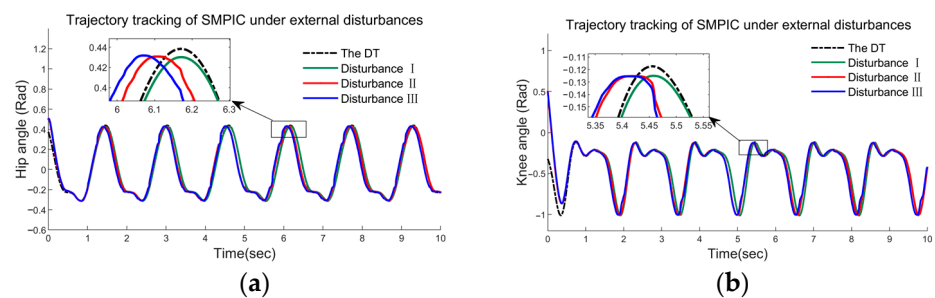


Figure 16. The tracking response of SMPIC of the joints under Case III. (a) the response of θ_1 and (b) the response of θ_2 under the disturbances with different magnitudes.

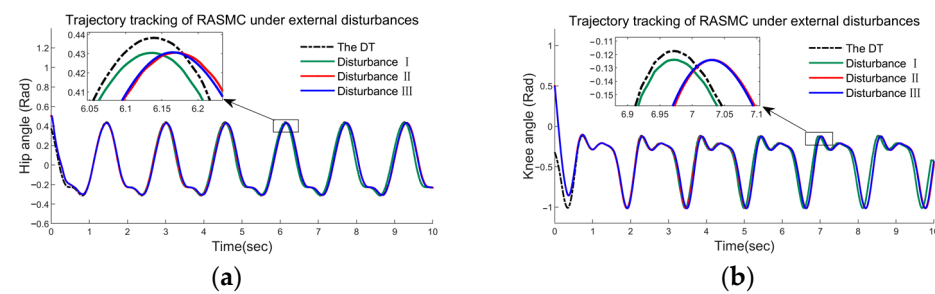


Figure 17. The tracking response of RASMC of the joints under Case III. (a) the response of θ_1 and (b) the response of θ_2 under the disturbances with different magnitudes.

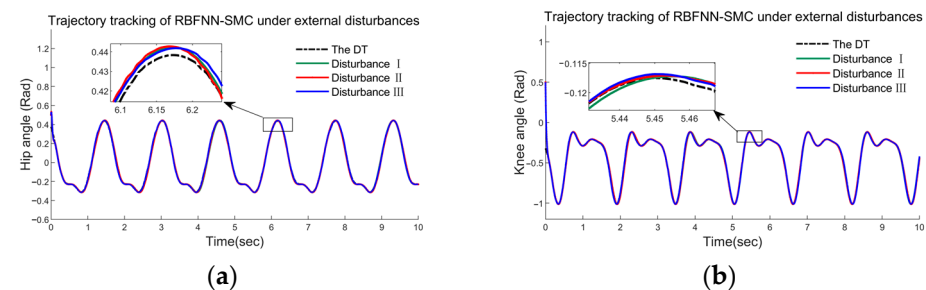


Figure 18. The tracking response of RBFNN-SMC of the joints under Case III. (a) the response of θ_1 and (b) the response of θ_2 under the disturbances with different magnitudes.

Finally, a step–response experiment was implemented to evaluate the stability and response speed of the proposed controller compared with SMPIC and RASMC. The experimental results are shown in Figure 19a,b. The results show that the proposed method responds quickly, and the tracking error can converge to zero in a relatively short period of time. As shown in Figure 19, the performance metrics, such as delay time and the rising

time of the proposed method, are in the range of approximately 0.1 to 0.2 s, while both SMPIC and RASMC are at 1 s or above.

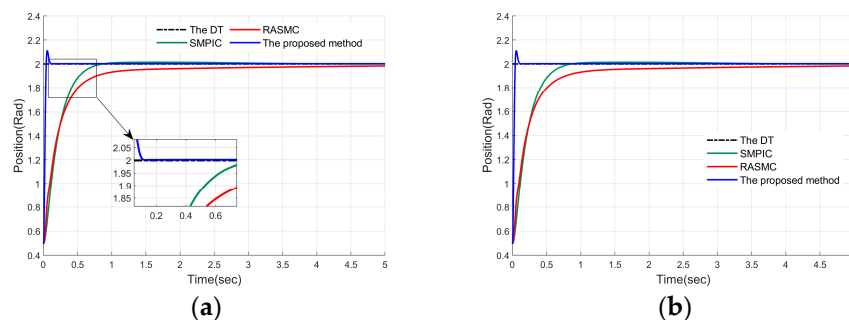


Figure 19. Comparison of controller response speed under step signals (a) the response speed of θ_1 and (b) the response speed of θ_2 .

In summary, compared with the other two controllers under different conditions, our proposed method can be efficiently adapted to track different trajectories and possess the fastest responding speed and the best tracking performance. In case I, case II, and case III, the robustness of our proposed method has been validated, which is extremely important in engineering practice. Regardless of all the cases, our proposed method is able to accurately complete trajectory tracking and overcome the effects of friction of CTSA while having a fast response speed and smooth torque output to meet the control requirements of CLLE effectively.

7. Conclusions

This paper investigated a robust adaptive sliding mode controller with an RBFNN compensator for 2-DOF CLLE. The model of CLLE was developed, and the model information for the hip and knee joints has been analyzed. Distinguishing from the previous research, the innovation of this paper is to investigate a novel robust adaptive SMC with RBFNN compensator, which can effectively approximate and compensate for the uncertainty and time-varying friction. In this paper, RASMC and SMPIC have been proposed to conduct comparative numerical simulations. All three methods have been proven by Lyapunov's method. The validation and performance of the proposed controller have been obtained by comparing it with SMPIC and RASMC. In the simulations, the proposed method claims the best tracking performance and fastest response speed compared with the other two methods. The proposed method possesses outstanding robustness and could achieve the purposes of CLLE for rehabilitation applications.

In future works, the validated experiments of the proposed control methods for the CLLE are on the schedule. The neural network algorithm is preparing to improve to achieve a more effective control strategy. More rigorous verification of the proposed controller in the future could be attempted in the underactuated exoskeleton and multiple actuation exoskeleton.

Author Contributions: Conceptualization, H.H. and Y.G.; Data curation, H.H.; Formal analysis, H.H. and Y.G.; Funding acquisition, R.X.; Investigation, H.H.; Methodology, H.H. and R.X.; Software, H.H.; Validation, H.H. and R.X.; Controller design, H.H. and R.X.; Controller construction, H.H. and R.X.; Visualization, H.H.; Writing—original draft, H.H. and R.X.; Writing—review & editing, H.H., R.X. and Y.G. All authors have read and agreed to the published version of the manuscript.

Funding: This research was supported by the National Natural Science Foundation of China Grant No. 51805128 and No. 51805475.

Institutional Review Board Statement: Not applicable.

Informed Consent Statement: Informed consent was obtained from all subjects involved in the study. Written informed consent has been obtained from the patient(s) to publish this paper.

Data Availability Statement: Not applicable.

Conflicts of Interest: The authors declare no conflict of interest.

References

1. Young, A.J.; Ferris, D.P. State of the Art and Future Directions for Lower Limb Robotic Exoskeletons. *IEEE Trans. Neural Syst. Rehabil. Eng.* **2017**, *25*, 171–182. [[CrossRef](#)] [[PubMed](#)]
2. Kapsalyamov, A.; Jamwal, P.K.; Hussain, S.; Ghayesh, M.H. State of the Art Lower Limb Robotic Exoskeletons for Elderly Assistance. *IEEE Access* **2019**, *7*, 95075–95086. [[CrossRef](#)]
3. Shakti, D.; Mathew, L.; Kumar, N.; Kataria, C. Effectiveness of robo-assisted lower limb rehabilitation for spastic patients: A systematic review. *Biosens. Bioelectron.* **2018**, *117*, 403–415. [[CrossRef](#)] [[PubMed](#)]
4. Pinto-Fernandez, D.; Torricelli, D.; del Carmen Sanchez-Villamanan, M.; Aller, F.; Mombaur, K.; Conti, R.; Vitiello, N.; Moreno, J.C.; Pons, J.L. Performance Evaluation of Lower Limb Exoskeletons: A Systematic Review. *IEEE Trans. Neural Syst. Rehabil. Eng.* **2020**, *28*, 1573–1583. [[CrossRef](#)]
5. Simbolotti, C.; Molteni, F.; Guanziroli, E.; Iacovelli, C.; Padua, L.; Cicetti, S.; Caloi, M.; Caliandro, P. Gait training with Ekso in ischemic chronic stroke patients: Effects on the timing of muscle activation and metabolic activation of the prefrontal cortex. *Gait Posture* **2016**, *49*, S27–S28. [[CrossRef](#)]
6. Tsukahara, A.; Hasegawa, Y.; Eguchi, K.; Sankai, Y. Restoration of Gait for Spinal Cord Injury Patients Using HAL with Intention Estimator for Preferable Swing Speed. *IEEE Trans. Neural Syst. Rehabil. Eng.* **2015**, *23*, 308–318. [[CrossRef](#)]
7. Buongiorno, D.; Sotgiu, E.; Leonardis, D.; Marcheschi, S.; Solazzi, M.; Frisoli, A. WRES: A Novel 3 DoF WRist ExoSkeleton with Tendon-Driven Differential Transmission for Neuro-Rehabilitation and Teleoperation. *IEEE Robot. Autom. Lett.* **2018**, *3*, 2152–2159. [[CrossRef](#)]
8. Jarrett, C.; Mcdaid, A.J. Robust Control of a Cable-Driven Soft Exoskeleton Joint for Intrinsic Human-Robot Interaction. *IEEE Trans. Neural Syst. Rehabil. Eng.* **2017**, *25*, 976–986. [[CrossRef](#)]
9. Cui, X.; Chen, W.; Jin, X.; Agrawal, S.K. Design of a 7-DOF Cable-Driven Arm Exoskeleton (CAREX-7) and a Controller for Dexterous Motion Training or Assistance. *IEEE/ASME Trans. Mechatron.* **2017**, *22*, 161–172. [[CrossRef](#)]
10. Hsieh, H.C.; Chen, D.F.; Chien, L.; Lan, C.C. Design of a Parallel Actuated Exoskeleton for Adaptive and Safe Robotic Shoulder Rehabilitation. *IEEE/ASME Trans. Mechatron.* **2017**, *22*, 2034–2045. [[CrossRef](#)]
11. Ding, Y.; Kim, M.; Kuindersma, S.; Walsh, C.J. Human-in-the-loop optimization of hip assistance with a soft exosuit during walking. *Sci. Robot.* **2018**, *3*, eaar5438. [[CrossRef](#)] [[PubMed](#)]
12. Quinlivan, B.T.; Lee, S.; Malcolm, P.; Rossi, D.M.; Grimmer, M.; Siviyy, C.; Karavas, N.; Wagner, D.; Asbeck, A.; Galiana, I.; et al. Assistance magnitude versus metabolic cost reductions for a tethered multiarticular soft exosuit. *Sci. Robot.* **2017**, *2*, eaah4416. [[CrossRef](#)] [[PubMed](#)]
13. Kapsalyamov, A.; Hussain, S.; Jamwal, P.K. State-of-the-Art Assistive Powered Upper Limb Exoskeletons for Elderly. *IEEE Access* **2020**, *8*, 178991–179001. [[CrossRef](#)]
14. Demofonti, A.; Carpino, G.; Zollo, L.; Johnson, M.J. Affordable Robotics for Upper Limb Stroke Rehabilitation in Developing Countries: A Systematic Review. *IEEE Trans. Med. Robot. Bionics* **2021**, *3*, 11–20. [[CrossRef](#)]
15. Hussain, S.; Jamwal, P.K.; Van Vliet, P.; Ghayesh, M.H. State-of-the-Art Robotic Devices for Wrist Rehabilitation: Design and Control Aspects. *IEEE Trans. Hum. Mach. Syst.* **2020**, *50*, 361–372. [[CrossRef](#)]
16. Wu, Q.; Wang, X.; Du, F.; Zhang, X. Design and Control of a Powered Hip Exoskeleton for Walking Assistance. *Int. J. Adv. Robot. Syst.* **2015**, *12*, 18. [[CrossRef](#)]
17. Rosales Luengas, Y.; López-Gutiérrez, R.; Salazar, S.; Lozano, R. Robust controls for upper limb exoskeleton, real-time results. *Proc. Inst. Mech. Eng. Part I J. Syst. Control Eng.* **2018**, *232*, 797–806. [[CrossRef](#)]
18. Sharma, R.; Gaur, P.; Bhatt, S.; Joshi, D. Optimal fuzzy logic-based control strategy for lower limb rehabilitation exoskeleton. *Appl. Soft Comput.* **2021**, *105*, 107226. [[CrossRef](#)]
19. Zhang, G.; Wang, J.; Yang, P.; Guo, S. A learning control scheme for upper-limb exoskeleton via adaptive sliding mode technique. *Mechatronics* **2022**, *86*, 102832. [[CrossRef](#)]
20. Razzaghian, A. A fuzzy neural network-based fractional-order Lyapunov-based robust control strategy for exoskeleton robots: Application in upper-limb rehabilitation. *Math. Comput. Simul.* **2022**, *193*, 567–583. [[CrossRef](#)]
21. Wu, Q.; Wu, H. Development, Dynamic Modeling, and Multi-Modal Control of a Therapeutic Exoskeleton for Upper Limb Rehabilitation Training. *Sensors* **2018**, *18*, 3611. [[CrossRef](#)] [[PubMed](#)]
22. Zhang, Y.; Cao, G.; Li, W.; Chen, J.; Li, L.; Diao, D. A Self-Adaptive-Coefficient-Double-Power Sliding Mode Control Method for Lower Limb Rehabilitation Exoskeleton Robot. *Appl. Sci.* **2021**, *11*, 10329. [[CrossRef](#)]
23. Yang, M.; Zhang, X.; Xia, Y.; Liu, Q.; Zhu, Q. Adaptive neural network-based sliding mode control for a hydraulic rotary drive joint. *Comput. Electr. Eng.* **2022**, *102*, 108189. [[CrossRef](#)]
24. Wang, J.; Liu, J.; Zhang, G.; Guo, S. Periodic event-triggered sliding mode control for lower limb exoskeleton based on human-robot cooperation. *ISA Trans.* **2022**, *123*, 87–97. [[CrossRef](#)]
25. Ghosh-Dastidar, S.; Adeli, H.; Dadmehr, N. Principal Component Analysis-Enhanced Cosine Radial Basis Function Neural Network for Robust Epilepsy and Seizure Detection. *IEEE Trans. Biomed. Eng.* **2008**, *55*, 512–518. [[CrossRef](#)] [[PubMed](#)]

26. Yang, R.; Yang, C.; Chen, M.; Annamalai, A.S. Discrete-time optimal adaptive RBFNN control for robot manipulators with uncertain dynamics. *Neurocomputing* **2017**, *234*, 107–115. [[CrossRef](#)]
27. Liu, Q.; Li, D.; Ge, S.S.; Ji, R.; Ouyang, Z.; Tee, K.P. Adaptive bias RBF neural network control for a robotic manipulator. *Neurocomputing* **2021**, *447*, 213–223. [[CrossRef](#)]
28. Mefoued, S. A second order sliding mode control and a neural network to drive a knee joint actuated orthosis. *Neurocomputing* **2015**, *155*, 71–79. [[CrossRef](#)]
29. Spong, M.W. *Robot Dynamics and Control*; John Wiley & Sons: Hoboken, NJ, USA, 1989.
30. Palli, G.; Melchiorri, C. Model and control of tendon-sheath transmission systems. In Proceedings of the 2006 IEEE International Conference on Robotics and Automation, San Diego, CA, USA, 13–15 December 2006; pp. 988–993.
31. Kaneko, M.; Wada, M.; Maekawa, H.; Tanie, K. A new consideration on tendon-tension control system of robot hands. In Proceedings of the 1991 IEEE International Conference on Robotics and Automation, Sacramento, CA, USA, 9–11 April 1991; Volume 2, pp. 1028–1033.
32. Xi, R.; Wang, X.; Lu, J.; Sheng, C. Modeling of Transmission Characteristics for a Tendon-sheath Actuation System. *Chin. J. Mech. Eng.* **2012**, *48*, 38–44. [[CrossRef](#)]
33. Shen, X.; Wang, X.; Tian, M.; Zhang, Q. Modeling and sensorless force control of novel tendon-sheath artificial muscle based on hill muscle model. *Mechatronics* **2019**, *62*, 102243. [[CrossRef](#)]
34. Wu, Q.; Wang, X.; Chen, L.; Du, F. Transmission Model and Compensation Control of Double-Tendon-Sheath Actuation System. *IEEE Trans. Ind. Electron.* **2015**, *62*, 1599–1609. [[CrossRef](#)]
35. Shao, Z.; Wu, Q.; Chen, B.; Wu, H.; Zhang, Y. Modeling and inverse control of a compliant single-tendon-sheath artificial tendon actuator with bending angle compensation. *Mechatronics* **2019**, *63*, 102262. [[CrossRef](#)]
36. Din, S.U.; Khan, Q.; Rehman, F.U.; Akmeiliawanti, R. A Comparative Experimental Study of Robust Sliding Mode Control Strategies for Underactuated Systems. *IEEE Access* **2017**, *5*, 10068–10080. [[CrossRef](#)]
37. Slotine, J.J.; Li, W. *Applied Nonlinear Control*; Prentice Hall: Englewood Cliffs, NJ, USA, 1991; Volume 199.
38. Yang, P.; Zhang, G.; Wang, J.; Wang, X.; Zhang, L.; Chen, L. Command Filter Backstepping Sliding Model Control for Lower-Limb Exoskeleton. *Math. Probl. Eng.* **2017**, *2017*, 1064535. [[CrossRef](#)]